


Cite this: *Chem. Sci.*, 2025, 16, 3168

All publication charges for this article have been paid for by the Royal Society of Chemistry

From 0D to 2D: microwave-assisted synthesis of electrically conductive metal–organic frameworks with controlled morphologies†

Xiaoyu Fang,^a Ji Yong Choi,^a Chenwei Lu,^a Elizabeth Reichert,^b Hoai T. B. Pham^a and Jihye Park  ^{*a}

Morphology control of electrically conductive metal–organic frameworks (EC-MOFs) can be a powerful means to tune their surface area and carrier transport pathways, particularly beneficial for energy conversion and storage. However, controlling EC-MOFs' morphology is underexplored due to the uncontrollable crystal nucleation and rapid growth kinetics. This work introduces a microwave-assisted strategy to readily synthesize Cu-HHTP (HHTP = 2,3,6,7,10,11-hexahydroxytriphenylene) with controlled morphologies. We controlled solvent compositions to facilitate particles' directional growth to 1D and 2D crystals. Meanwhile, we found that ultrasonication can manipulate crystal seeding, yielding 0D spherical Cu-HHTP crystals. Electronic conductivity measurements suggest that the isotropic nature of the 0D crystals allows a conductivity of $7.34 \times 10^{-1} \text{ S cm}^{-1}$, much higher than 1D and 2D counterparts. Additionally, the controlled 0D morphology enhanced the material's capacitance and effective surface area and significantly improved its photocurrent response. These findings underscore the pivotal impact of controlled morphology in optimizing EC-MOFs' physicochemical properties.

Received 16th October 2024

Accepted 12th January 2025

DOI: 10.1039/d4sc07025a

rsc.li/chemical-science

Introduction

Electrically conductive metal–organic frameworks (EC-MOFs) represent a class of porous solids that combine the design flexibility of conventional MOFs and electronic conduction properties, making them promising for energy conversion and storage.^{1–4} To optimize their performance, a common strategy is to tailor their electronic structure and charge transport through linker and metal node designs.^{5–10} Morphology control has proven to enhance mass transport by exposing specific crystal facets that increase substrate accessibility or active sites in MOFs.^{11–15} However, the current EC-MOFs' synthetic strategies are predominantly *via* conventional solvothermal methods, which pose substantial challenges in controlling EC-MOFs' synthesis due to faster growth kinetics than conventional MOFs.^{16–18}

EC-MOFs usually employ organic linkers containing hydroxy (–OH) or amino (–NH₂) groups to ensure electronic conductivity *via* d–p conjugation with metal nodes, often resulting in a 2D sheet made of strong metal-linker conjugation.^{1,19–21} However, such strong interactions in in-plane growth are energetically

demanding and less reversible, making it difficult to achieve consistent and extensive growth in the *ab* plane. In contrast, weaker interlayer interactions promote the growth along the *c*-axis, typically leading to a 1D rod morphology.^{19,22} Leveraging on such unique properties of EC-MOFs, common strategies include suppressing the rate of in-plane growth (*ab* plane) or enhancing out-of-plane growth (*c*-axis) to control EC-MOFs' morphology.^{23,24} Forse and co-workers demonstrated morphology control of Cu-HHTP using modulators such as NH₃ and pyridine.²⁵ Xiao and co-workers also achieved morphology control *via* control of the linker's oxidation state, which influenced the nucleation and growth of Cu-HHTP.¹² Additionally, top-down approaches have been employed: Dincă and co-workers controlled the nucleation to produce large Cu-HHTP particles, then exfoliated them into 2D flakes.²⁶

Taking a different strategy from the above manipulating growth rates in different directions, our group has recently reported an electrochemical method to tailor EC-MOF morphologies.²⁷ This method allowed for controlling nucleation and precipitation rates by varying the concentration of HHTP linkers, resulting in two distinct morphologies (Ni-HHTP-Flower and Ni-HHTP-Disc) on Ni foam, showing different electrochemical active surface area (ECSA).

In this work, we have explored other approaches to precisely controlling morphologies. Microwave synthesis is unique from conventional hydrothermal methods because of its rapid and uniform heating advantages. This advantage could significantly

^aDepartment of Chemistry, University of Colorado Boulder, Boulder, Colorado 80303, USA. E-mail: Jihye.Park@colorado.edu

^bChemical and Biological Engineering, University of Colorado Boulder, Boulder, Colorado 80303, USA

† Electronic supplementary information (ESI) available. See DOI: <https://doi.org/10.1039/d4sc07025a>

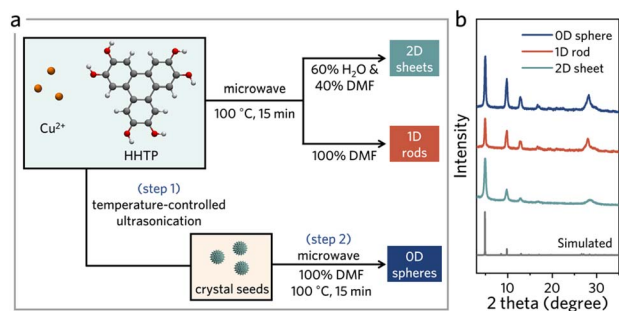


Fig. 1 (a) Schematic of the synthesis of 0D, 1D, and 2D Cu-HHTP based on microwave and temperature-controlled ultrasonication treatment. (b) PXRD patterns of 0D, 1D, and 2D from the respective synthetic methods. The gray line indicates the simulated PXRD pattern.

influence crystal growth and morphology through accelerated reaction kinetics and enhanced nucleation uniformity.^{28–30}

However, this method has yet to be widely applied to synthesize EC-MOFs, possibly due to the limited understanding of the crystallization process of EC-MOFs under microwave conditions. Herein, we report a microwave-assisted strategy that can selectively shape Cu-HHTP particles into 1D or 2D morphologies (Fig. 1). We then coupled microwave synthesis with ultrasonication at varied temperatures to achieve highly dispersed seed clusters. Subsequent microwave treatment transformed these seeds into microscale 0D Cu-HHTP, which features a larger surface area and higher electronic conductivity than their 1D and 2D counterparts.

Results and discussion

Synthesis of Cu-HHTP with different morphologies

Based on the solvothermal synthesis conditions, we developed a microwave-assisted strategy that efficiently synthesizes Cu-HHTP in various morphologies (Fig. 1a). We optimized the key microwave reaction parameters, including temperature, reaction time, and solvent composition, to control the morphological outcomes (Fig. S1–S3†). By varying the ratio of water and *N,N*-dimethylformamide (DMF) in the reaction, we achieved a transition from 1D to 2D morphology within 15 min. This significantly reduced the reaction time from 24 h, typically required by conventional hydrothermal methods,²⁵ while yielding high crystalline products. Specifically, a 100% DMF solvent results in rod-like 1D morphology (Fig. 1a, 2b and S4†), while a mixture of 60% H₂O and 40% DMF produces 2D sheet-like morphology (Fig. 1a, 2c and S4†). In short, microwave-assisted synthesis not only expedited the synthesis but allowed for fine control over the morphologies of the synthesized EC-MOFs by simply varying the solvent composition. The powder X-ray diffraction (PXRD) patterns indicated that the synthesized Cu-HHTPs, across all morphologies (0D, 1D, and 2D), can match the simulation data well without impurities (Fig. 1b, S5, S6 and Table S1†). The 1D form, in particular, shows a pronounced diffraction peak at *ca.* 28°, suggesting more substantial stacking along the *c*-axis (Fig. 1b and S7†).³¹ Scanning electron microscopy-energy dispersive spectroscopy

(SEM-EDS) analysis showed that Cu, C, and O were uniformly distributed throughout the synthesized Cu-HHTP (Fig. S8†), and that their elemental ratios closely matched the predicted values (Table S2†), also confirming the successful formation of the desired Cu-HHTP structure with the intended stoichiometry.

Building on this foundation, we explored temperature-controlled ultrasonication to refine the morphology of Cu-HHTP further. We hypothesized that cooling the reaction temperature below room temperature could stall the crystal seed growth while ultrasonication could facilitate the crystal seeds' dispersion. Dispersing seeds well is expected to promote uniform Cu-HHTP morphology. Following the microwave treatment, we obtained a previously unreported spherical morphology of Cu-HHTP (*ca.* *d* = 3.55 μm) from 100% DMF as the solvent (Fig. 2a, see ESI for synthesis, Fig. S1–S3†). The magnified SEM images revealed that a small number of 0D crystals comprised smaller 1D rods, possibly indicating that these 0D crystals are constructed from basic units of 1D rods (Fig. S9†). The resulting PXRD pattern of 0D Cu-HHTP exhibited a pronounced stacking feature, similar to 1D Cu-HHTP, as they constitute the 0D sphere (Fig. 1b). N₂ sorption measurements indicate that the 0D MOF exhibits the largest Brunauer–Emmett–Teller (BET) surface area of 789.72 m² g^{−1}, around twice that of 1D and 2D counterparts (Fig. 2 and S10†). Full-width at half-maximum (FWHM) at 4.93° is similar across the samples (Table S3†), suggesting a comparable degree of defects across 0D, 1D, and 2D Cu-HHTPs. Thus, the significant increase in surface area may be due to the enhanced stacking, which preserves long-range pore order and fully exposes the internal channels, thereby improving their accessibility.

Growth mechanism

To better understand the growth mechanism of 0D Cu-HHTP particles, we used SEM to monitor their morphology evolution at different growth stages. Early observation after ultrasonication revealed the formation of seed clusters, evidenced by the Tyndall effect in the reaction solution, indicating a colloidal system (Fig. S11†). This effect resulted from ultrasonication at controlled temperatures, which rapidly produced high concentrations of crystal seeds, more than those typically achieved with conventional heating.

As the growth proceeds under the microwave treatment (100–200 W), these seeds began to organize into sea urchin-like structures, with 1D crystals radiating outward from the center (Fig. 3a). Over time, the length of and cross-sectional diameter of the 1D rods continue to increase (Fig. 3b and c). An increase in 1D rod length contributed to the overall growth in the diameter of the spherical particles, from approximately 0.70 μm at 5 min to 3.55 μm at 15 min. The increase in the diameter of the 1D rods also led to a smooth surface of the spherical particles (Fig. 3c). This process presents the importance of controlled seeding and growth directionality, facilitated by a combination of ultrasonication and microwave treatment. The orderly expansion of these 1D structures from seed clusters ultimately resulted in the formation of spherical 0D Cu-HHTP crystals with distinct morphological characteristics.



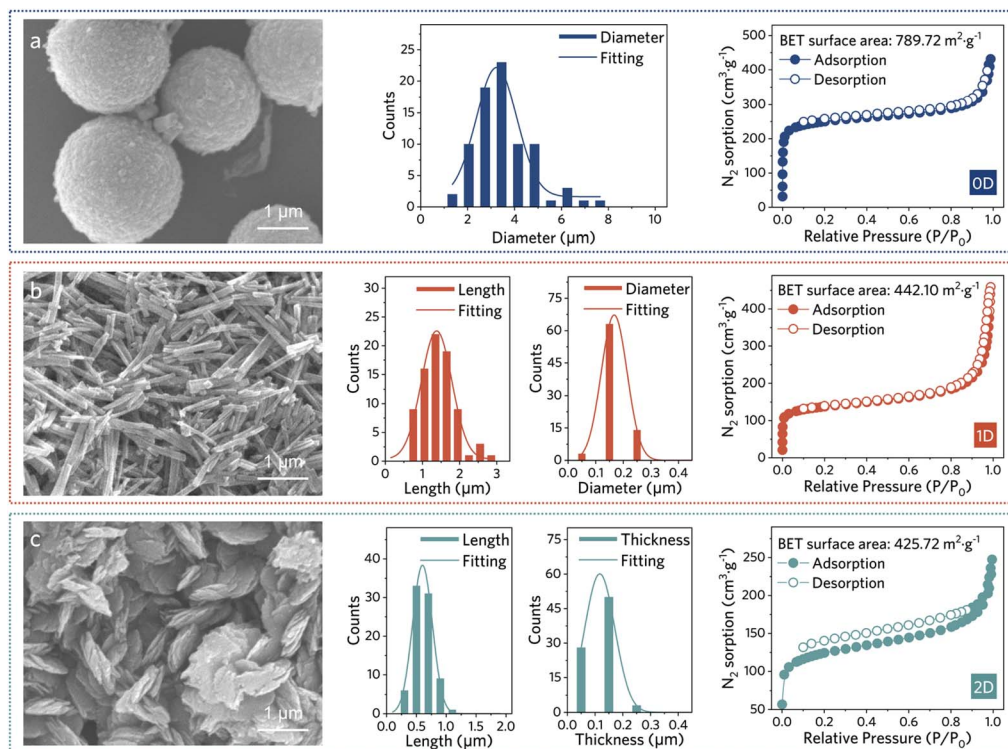


Fig. 2 SEM images, diameter/length/thickness distributions, and nitrogen sorption isotherms for (a) 0D, (b) 1D, and (c) 2D Cu-HHTP.

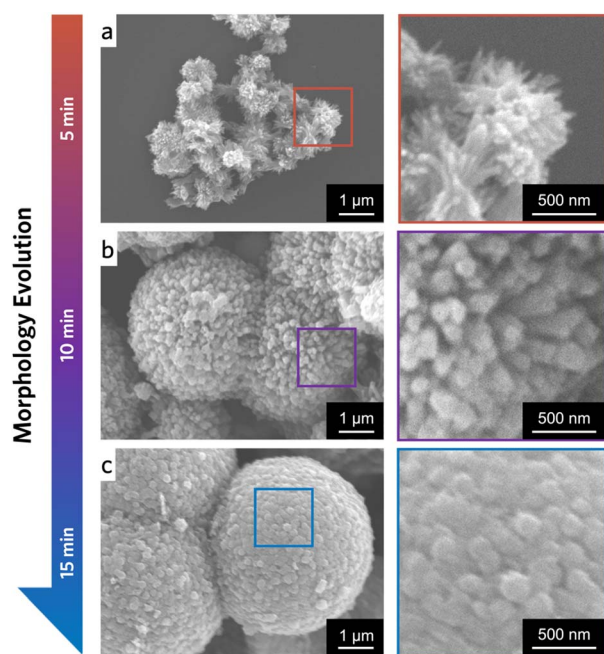


Fig. 3 SEM images for 0D spheres at (a) 5 min, (b) 10 min, and (c) 15 min. The corresponding magnified views of a single particle's surface are on the right.

To gain insights into the 0D Cu-HHTP growth, we decreased the concentrations of Cu^{2+} and HHTP. With this, we expected to minimize the formation of dense seed clusters, thereby facilitating the observation of individual growth. When the

concentration was reduced to half of the original experiment, we captured fragments of the 0D particles *via* SEM. Observing the SEM images, the Cu-HHTP crystals grew from the focal point to the periphery, corroborating our proposed growth mechanism (Fig. S12a and b†). At the same time, due to the lower concentration of the reactants, the size of the Cu-HHTP crystals increased significantly, and the constituting rods of the 0D spheres reached $\sim 15 \mu\text{m}$ (Fig. S12c†). This observation aligns well with the nucleation density to control crystal sizes, where reducing the concentration tends to result in large-scale crystal formation.³²

Electronic transport properties

The conductivity of powder Cu-HHTP from traditional methods (*e.g.*, hydrothermal method) is often much lower than that of single-crystalline Cu-HHTP, which can reach up to 1.5 S cm^{-1} for 1D rods and 0.5 S cm^{-1} for 2D sheets (Table S4†).²⁶ This difference is primarily due to the interparticle transport barrier.³³ Additionally, the rapid crystal growth inevitably leads to surface or internal defects. Together, these transport barriers contribute to the lower conductivity of powder Cu-HHTP than single crystals, limiting the advantage of electronic conduction in Cu-HHTP.³⁴

Surprisingly, the 0D Cu-HHTP spheres show an electronic conductivity close to that of single crystal Cu-HHTP, reaching $7.34 \times 10^{-1} \text{ S cm}^{-1}$ (Fig. 4a and Table S4†). It is nearly one order of magnitude higher than the 1D and 2D powders prepared by the same microwave-assisted strategy ($3.00 \times 10^{-2} \text{ S cm}^{-1}$ for 1D and $2.70 \times 10^{-2} \text{ S cm}^{-1}$ for 2D). We rationalize that superior

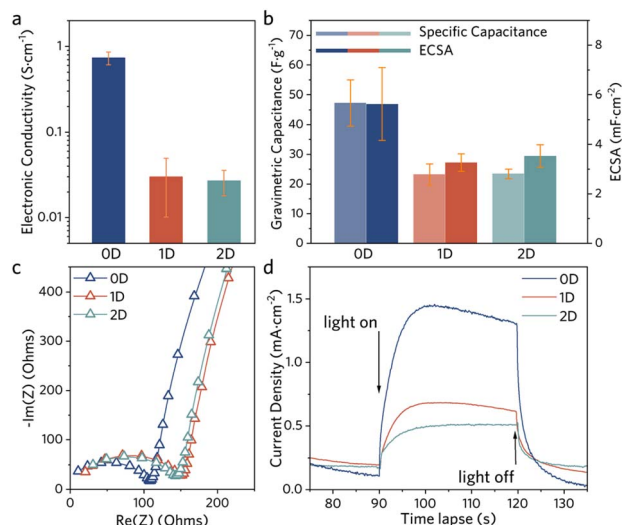


Fig. 4 (a) Electrical conductivity of 0D, 1D, and 2D Cu-HHTP. (b) Bar graph showing the gravimetric capacitance (light colors) and ECSA (dark colors) of 0D, 1D, and 2D Cu-HHTP. (c) EIS and (d) transient photocurrent response of 0D, 1D, and 2D Cu-HHTP.

electronic conductivity is closely linked to the 0D morphology. Since the 1D rods grew uniformly from the center of the 0D sphere to the periphery, the electrons can be conducted along the *c*-axis within each rod of the single 0D particle. Therefore, the 0D crystals show isotropic electronic transport between particles *via* out-of-plane conductivity (Fig. S13[†]). Previous studies have shown that the in-plane and out-of-plane conductivity of Cu-HHTP are comparable in magnitude, supporting our rationale.^{19,26} We expected this isotropic electronic transport would reduce the anisotropic charge transport barrier compared to 1D and 2D powders, providing more efficient pathways in the pelletized form. Our findings underscore the potential of 0D Cu-HHTP to enhance electronic conduction in the powdered forms of this material.

Electrochemical characterization

We evaluated the electrochemical features of the synthesized Cu-HHTPs with various morphologies. We expect the morphology to enhance charge storage and efficient adsorption. The cyclic voltammetry (CV) curves reveal a feature at -1.1 V vs. Ag/AgCl across all samples (Fig. S14a[†]), aligning with the redox properties of the HHTP linker.³⁴ However, 0D Cu-HHTP showed a larger capacitance, measured at 47.27 F g^{-1} (Fig. 4b). The trend of the 0D sphere's capacitance greater than 1D and 2D positively correlates with the BET surface areas. The 0D morphology exhibits the highest capacitance, which may seem contradictory to a previous study by Forse *et al.* However, we believe that our results can be attributed to the highly ordered hierarchical structure of our spherical morphology, which is made up of highly crystalline rods, which facilitated access to the internal pores.³⁰

Additionally, CV measurements at different scan rates confirmed that the ECSA of 0D Cu-HHTP is significantly higher, measuring 5.63 mF cm^{-2} , compared to 3.26 mF cm^{-2} for 1D and

3.53 mF cm^{-2} for 2D counterparts (Fig. 4b, S14b and S15[†]). The ECSA results indicate the efficient accessibility of the internal pores of 0D Cu-HHTP. Electrochemical impedance spectroscopy (EIS) data indicate less resistance for 0D Cu-HHTP than 1D and 2D counterparts (Fig. 4c), consistent with electrical conductivity measured by the four-point probe method.

We also monitored the transient photocurrent response of these three morphologies. Since the three different morphologies of Cu-HHTP show similar absorption profiles in UV-vis spectroscopy (Fig. S16[†]), we use xenon light to simulate sunlight for the photocurrent measurement. All three samples generate photogenerated currents where the 0D morphology shows a significantly higher current than the other two morphologies (Fig. 4d). The results support the higher conductivity of the 0D crystals for photogenerated carrier transport.

Conclusion

In summary, we report synthetic strategies for tuning EC-MOF morphologies, providing an effective alternative to conventional solvothermal methods. Specifically, we utilize microwave-assisted and temperature-controlled ultrasonication methods to customize morphologies of Cu-HHTP, including 0D, 1D, and 2D crystals. The microwave-assisted synthesis provides excellent morphological control, enabling rapid acquisition of uniform EC-MOF particles' morphology. Meanwhile, temperature-controlled ultrasonication adjusts EC-MOF crystal seeds' concentration and dispersion, inducing new growth trends distinct from adding chemical modulators. We demonstrate that 0D Cu-HHTP exhibits isotropic electron transport, exhibiting electronic conductivity nearing those of single-crystal EC-Cu-HHTPs. Moreover, 0D Cu-HHTP shows superior photo(electro)chemical performance compared to its 1D and 2D counterparts, attributing enhanced properties to controlled synthetic morphologies. Our strategies precisely control the synthesis conditions and morphologies of EC-MOFs, contributing to the existing body of knowledge to unlock their potential in energy conversion and storage as synthetic knobs.

Data availability

The data supporting this article have been included as part of ESI.[†]

Author contributions

X. F. and J. P. designed and organized the project. X. F. conducted most characterizations. X. F., J. Y. C., and E. R. contributed to the synthesis of Cu-HHTP. C. L. provided the organic linkers. X. F., J. Y. C., H. T. B. P., and J. P. wrote the manuscript. All authors contributed to writing the manuscript.

Conflicts of interest

There are no conflicts to declare.



Acknowledgements

J. P. acknowledges the Office of Naval Research under award no. N00014-24-1-2112. H. T. B. P. acknowledges support from the Graduate Research Fellowship Program from the National Science Foundation of the United States under Grant No. DGE 2040434.

Notes and references

- 1 L. S. Xie, G. Skorupskii and M. Dincă, *Chem. Rev.*, 2020, **120**, 8536–8580.
- 2 X. Fang, J. Y. Choi, M. Stodolka, H. T. B. Pham and J. Park, *Acc. Chem. Res.*, 2024, **57**, 2316–2325.
- 3 A. Schneemann, R. Dong, F. Schwotzer, H. Zhong, I. Senkovska, X. Feng and S. Kaskel, *Chem. Sci.*, 2021, **12**, 1600–1619.
- 4 M. Wang, R. Dong and X. Feng, *Chem. Soc. Rev.*, 2021, **50**, 2764–2793.
- 5 C. Lu, B. Clayville, J. Y. Choi and J. Park, *Chem*, 2023, **9**, 2757–2770.
- 6 Y. Lu, P. Samorì and X. Feng, *Acc. Chem. Res.*, 2024, **57**, 1985–1996.
- 7 J. Y. Choi, M. Wang, B. Check, M. Stodolka, K. Tayman, S. Sharma and J. Park, *Small*, 2023, **19**, 2206988.
- 8 Z. Meng, J. Luo, W. Li and K. A. Mirica, *J. Am. Chem. Soc.*, 2020, **142**, 21656–21669.
- 9 P. Apostol, S. M. Gali, A. Su, D. Tie, Y. Zhang, S. Pal, X. Lin, V. R. Bakuru, D. Rambabu, D. Beljonne, M. Dincă and A. Vlad, *J. Am. Chem. Soc.*, 2023, **145**, 24669–24677.
- 10 A. M. Eagleton, M. Ko, R. M. Stolz, N. Vereshchuk, Z. Meng, L. Mendecki, A. M. Levenson, C. Huang, K. C. MacVeagh, A. Mahdavi-Shakib, J. J. Mahle, G. W. Peterson, B. G. Frederick and K. A. Mirica, *J. Am. Chem. Soc.*, 2022, **144**, 23297–23312.
- 11 J. M. Wrogemann, M. J. Lüther, P. Bärmann, M. Lounasvuori, A. Javed, M. Tiemann, R. Golnak, J. Xiao, T. Petit, T. Placke and M. Winter, *Angew. Chem., Int. Ed.*, 2023, **62**, e202303111.
- 12 M. Adam Borysiewicz, J.-H. Dou, I. Stassen and M. Dincă, *Faraday Discuss.*, 2021, **231**, 298–304.
- 13 K. M. Snook, L. B. Zasada, D. Chehada and D. J. Xiao, *Chem. Sci.*, 2022, **13**, 10472–10478.
- 14 B. C. Bukowski, F. A. Son, Y. Chen, L. Robison, T. Islamoglu, R. Q. Snurr and O. K. Farha, *Chem. Mater.*, 2022, **34**, 4134–4141.
- 15 F. Zhan, H. Wang, Q. He, W. Xu, J. Chen, X. Ren, H. Wang, S. Liu, M. Han, Y. Yamauchi and L. Chen, *Chem. Sci.*, 2022, **13**, 11981–12015.
- 16 H. Meng, Y. Han, C. Zhou, Q. Jiang, X. Shi, C. Zhan and R. Zhang, *Small Methods*, 2020, **4**, 2000396.
- 17 L. Niu, T. Wu, M. Chen, L. Yang, J. Yang, Z. Wang, A. A. Kornyshev, H. Jiang, S. Bi and G. Feng, *Adv. Mater.*, 2022, **34**, 2200999.
- 18 Q. Jiang, C. Zhou, H. Meng, Y. Han, X. Shi, C. Zhan and R. Zhang, *J. Mater. Chem. A*, 2020, **8**, 15271–15301.
- 19 J.-H. Dou, M. Q. Arguilla, Y. Luo, J. Li, W. Zhang, L. Sun, J. L. Mancuso, L. Yang, T. Chen, L. R. Parent, G. Skorupskii, N. J. Libretto, C. Sun, M. C. Yang, P. V. Dip, E. J. Brignole, J. T. Miller, J. Kong, C. H. Hendon, J. Sun and M. Dincă, *Nat. Mater.*, 2021, **20**, 222–228.
- 20 H. T. B. Pham, J. Y. Choi, M. Stodolka and J. Park, *Acc. Chem. Res.*, 2024, **57**, 580–589.
- 21 J. Liu, X. Song, T. Zhang, S. Liu, H. Wen and L. Chen, *Angew. Chem., Int. Ed.*, 2021, **133**, 5672–5684.
- 22 Y. Mu, J. Nyakuchena, Y. Wang, J. R. Wilkes, T. Luo, M. Goldstein, B. Elander, U. Mohanty, J. L. Bao, J. Huang and D. Wang, *Angew. Chem., Int. Ed.*, 2024, e202409286.
- 23 X. Wang, X. Zhang, A. He, J. Guo and Z. Liu, *Inorg. Chem.*, 2024, **63**, 6948–6956.
- 24 M. Ko, L. Mendecki, A. M. Eagleton, C. G. Durbin, R. M. Stolz, Z. Meng and K. A. Mirica, *J. Am. Chem. Soc.*, 2020, **142**, 11717–11733.
- 25 J. W. Gittins, C. J. Balhatchet, S. M. Fairclough and A. C. Forse, *Chem. Sci.*, 2022, **13**, 9210–9219.
- 26 R. W. Day, D. K. Bediako, M. Rezaee, L. R. Parent, G. Skorupskii, M. Q. Arguilla, C. H. Hendon, I. Stassen, N. C. Gianneschi, P. Kim and M. Dincă, *ACS Cent. Sci.*, 2019, **5**, 1959–1964.
- 27 M. Stodolka, J. Y. Choi, X. Fang, C. Lu, H. T. B. Pham, B. Check and J. Park, *ACS Mater. Lett.*, 2024, **6**, 49–55.
- 28 H. Qiao, M. T. Saray, X. Wang, S. Xu, G. Chen, Z. Huang, C. Chen, G. Zhong, Q. Dong, M. Hong, H. Xie, R. Shahbazian-Yassar and L. Hu, *ACS Nano*, 2021, **15**, 14928–14937.
- 29 N. Devi, S. Sahoo, R. Kumar and R. Kumar Singh, *Nanoscale*, 2021, **13**, 11679–11711.
- 30 C. Chen, X. Feng, Q. Zhu, R. Dong, R. Yang, Y. Cheng and C. He, *Inorg. Chem.*, 2019, **58**, 2717–2728.
- 31 Z.-Z. Ma, Q.-H. Li, Z. Wang, Z.-G. Gu and J. Zhang, *Nat. Commun.*, 2022, **13**, 6347.
- 32 Y. Zhang, R. Wang and Z. Tan, *J. Mater. Chem. A*, 2023, **11**, 11607–11636.
- 33 E. M. Johnson, S. Ilic and A. J. Morris, *ACS Cent. Sci.*, 2021, **7**, 445–453.
- 34 J. Y. Choi and J. Park, *ACS Appl. Electron. Mater.*, 2021, **3**, 4197–4202.

